Materials Today Bio 16 (2022) 100376

Contents lists available at ScienceDirect

Materials Today Bio

journal homepage: www.journals.elsevier.com/materials-today-bio

Fabrication of high-strength, flexible, porous collagen-based scaffolds to promote tissue regeneration

Xiaotang He [a], Wen Li [b], Siyang Liu [b], Yi Li [b], Yining Chen [a], Nianhua Dan [a], Weihua Dan [a,**], Meifeng Zhu [b,c,*]

[a] Key Laboratory of Leather Chemistry and Engineering (Sichuan University), Ministry of Education, Chengdu, 610065, PR China
[b] College of Life Sciences, Key Laboratory of Bioactive Materials (Ministry of Education), State Key Laboratory of Medicinal Chemical Biology, Nankai University, Tianjin, 300071, China
[c] Haihe Laboratory of Sustainable Chemical Transformations, Tianjin, 300192 China

ARTICLE INFO

Keywords:
Collagen
High-strength
Flexible
Porous scaffolds
Tissue regeneration

ABSTRACT

Collagen-based scaffolds lack mechanical strength, flexibility, and tunable pore structure, affecting tissue repair outcomes and restricting their wide clinical application. Here, two kinds of scaffolds were prepared by a combination of vacuum homogenization, natural air drying, water soaking, lyophilization, and crosslinking. Compared with the scaffolds made of collagen molecules (Col-M), the scaffolds made of collagen aggregates (Col-A) exhibited higher mechanical strength (ultimate tensile strength: 1.38 ± 0.26 MPa *vs* 15.46 ± 1.55 MPa), stronger flexibility, advanced cell adhesion, survival, and proliferation. Subcutaneous implantation in rats showed that Col-A scaffolds promoted cell infiltration, macrophage polarization, and vascularization. Furthermore, the Col-A scaffolds inhibited abdominal bulges due to their adequate mechanical support, and they also promoted vascularized muscle regeneration in a rat abdominal hernia defect model. Our study provides a novel strategy for generating high-strength, flexible, porous collagen-based scaffolds, which can be applied to tissue repair with mechanical strength requirements. It broadens their application range in the field of regenerative medicine.

1. Introduction

As a natural biomaterial, collagen has the advantages of good biocompatibility, weak antigenicity, and biodegradability [1]. However, the lack of mechanical strength and flexibility limits its wide application in tissue engineering and regenerative medicine [2,3]. Therefore, there is an urgent need to develop a new strategy to improve collagen-based scaffolds' mechanical strength and flexibility, which can be used for tissue repair in load-bearing sites such as hernias, tendons, blood vessels, dura mater, etc. [4]. In addition, suitable pore structure facilitates cell infiltration and vascularization, thereby promoting tissue restoration [5]. It remains a challenge to construct collagen scaffolds with high mechanical strength, flexibility, and controllable pore structure.

Up to now, numerous methods including physical, biological, and chemical cross-linking have been developed to improve the mechanical strength of collagen scaffolds, however, they also led to unexpected but inevitable results [6–11]. For example, dehydrothermal crosslinking causes the denaturation of collagen scaffolds. Materials treated with genipin were easily colored [12], and glutaraldehyde is cytotoxic and can lead to calcification *in vivo* [2]. The addition of inorganic materials (metal ions such as Ag^{+}, Ca^{2+}, Fe^{3+}, or graphene) increased brittleness and compromised collagen scaffolds' biocompatibility [13,14]. Incompatible issues often occur when mixing collagen with other natural materials, including cellulose nanofibers/nanocrystals, keratin, casein, gelatin, etc. [15]. Mechanical processing, such as rotational extrusion or plastic compression, usually generates collagen membrane with a dense structure, limiting cell migration and tissue regeneration [16,17]. Therefore, developing a new strategy to create high-strength, flexible, porous collagen scaffolds is urgently needed.

It is well known that collagen has a hierarchical structure, assembling from collagen molecules (1.5 nm in diameter) into microfibrils (10 nm), fibrils (10 nm −1 μm), fibers (>10 μm), and fascicles (>100 μm). Accordingly, their mechanical strength is highly correlated with growing levels of hierarchy assembly [18]. High-level collagens structures such as

* Corresponding author. College of Life Sciences, Key Laboratory of Bioactive Materials (Ministry of Education), State Key Laboratory of Medicinal Chemical Biology, Nankai University, Tianjin, 300071, China.
** Corresponding author.
E-mail addresses: danweihua@scu.edu.cn (W. Dan), 9920200134@nankai.edu.cn (M. Zhu).

https://doi.org/10.1016/j.mtbio.2022.100376
Received 8 May 2022; Received in revised form 18 July 2022; Accepted 19 July 2022
Available online 5 August 2022

the Achilles tendon are critical to mechanical properties, including significant extensibility, strain hardening, and toughness. However, single collagen molecules alone cannot provide this broad range of mechanical functionality [19]. We hypothesized that collagen aggregates were utilized to fabricate scaffolds to improve their mechanical strength and flexibility.

In this study, collagen aggregates were firstly extracted from bovine Achilles tendon and then made into high-strength, flexible, porous scaffolds (Col-A) through vacuum homogenization, natural air drying, water soaking, lyophilization, and cross-linking. The control scaffolds (Col-M) were made by collagen molecules with similar approach. The mechanical strength and flexibility of both scaffolds were evaluated. The cytocompatibility and histocompatibility of both scaffolds were verified *in vitro* and *in vivo*. The effects on tissue regeneration of both scaffolds were also evaluated using a ventral hernia repair model in rats (Fig. 1). This approach expands the application scope of collagen-based scaffolds in tissue engineering and regenerative medicine.

2. Materials and methods

2.1. Materials

Collagen molecules extracted from the bovine tendon by pepsin digestion (pH: 2–3) was supplied by Sannie Bioengineering Technology Co. Ltd. (Tianjin, China). 1-Ethyl-3-(3-dimethyl aminopropyl) carbodiimide (EDC) and *N*-hydroxysuccinimide (NHS) were supplied by Ziyi Reagent Ltd. (Shanghai, China). Analytical reagents, including acetic acid, sodium chloride, silver nitrate, and ethanol, were obtained from Tianjin Chemical Reagent Company (Tianjin, China).

2.2. Extraction of collagen aggregate

Collagen aggregates were extracted from the bovine tendon using the previously reported method with slight modification [20]. Briefly, the fascia and fat were firstly removed from the bovine tendon, and then they were cut into 1.0 mm slices and washed with purified water. Next, they were immersed in 0.5% chlorhexidine acetate and homogenized in a tissue homogenizer. Tissue homogenates were impregnated in 0.5 M acetic acid at a ratio of 1:50 (w/v) for 48 h (hrs) at 2–8 °C, with a gentle and continuous stirring to make the tissue fully swell up. Swollen tissue was separated by centrifugation at 8000 r/min for 15 min (min) at 4 °C. The sodium hydroxide solution was dripped into the retained supernatants to adjust pH to 7.5, followed by salted-out by adding NaCl at a final concentration of 10%. The resulting precipitates are collected by sieve. The precipitate was dialyzed against distilled water in a dialysis tube with a molecular weight cut-off of 80–140 kDa until a neutral pH was obtained. Finally, the collagen aggregates were successfully obtained after lyophilization.

2.3. Preparation of Col-A and Col-M scaffolds

The collagen aggregates (10 mg/ml) were immersed in deionized water for 24 h at 2–8 °C and then were homogenized three times under a vacuum for 20 s each time. For fabrication of Col-M and Col-A scaffolds, 1% of the collagen molecules and 1% of collagen aggregates were poured into a sieve with a diameter of 20 cm, respectively. Collagen aggregate homogenates covered by 80 mesh nylon net were slowly poured into a sieve with a diameter of 20 cm after removing air bubbles. Then they were dried to form a transparent membrane at room temperature. The membrane was immersed in deionized water for 1 h and 3 h (soaking

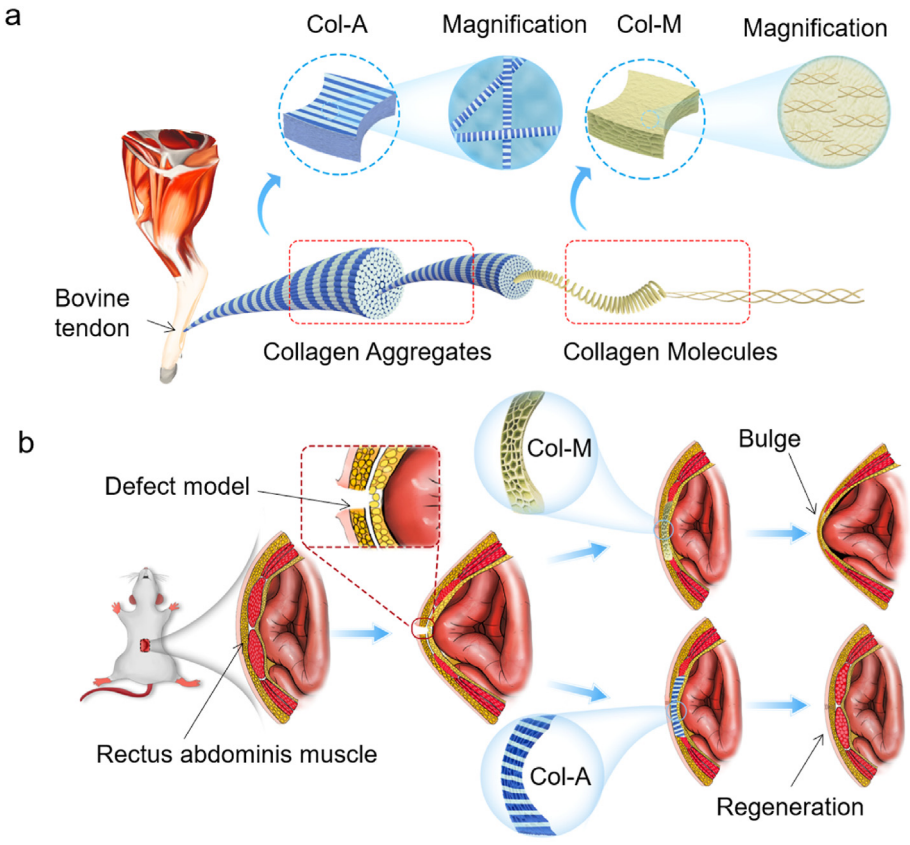

Fig. 1. Sketch map of generation and application of Col-A and Col-M scaffolds. (a) Schematic illustration showing collagens with different hierarchical architectures for fabricating scaffolds. (b) the scaffolds were applied to repair the ventral hernia model in rats.

time), and then freeze-dried after pre-freezing at −20 °C, −80 °C, and liquid nitrogen for 24 h. The freeze-dried membranes was immersed in 80% ethanol solution, and EDC and NHS were added to the solution to form a mixture with a mass ratio of NHS: EDC: membranes = 3:12:20. The freeze-dried membranes were chemically crosslinked by immersing in 80% ethanol solution containing a mixture of EDC and NHS for 4 h (crosslinking time). Purified water was used to remove the residual EDC/NHS. After that, the Col-A scaffolds were freeze-dried for 48 h after rinsing with deionized water for 48 h. The Col-M scaffolds made of collagen molecules were also fabricated with this process.

2.4. Scanning electron microscopy (SEM) and pore size measurements

The top surface and cross section of scaffolds were attached on the sample table with conductive adhesive and sputter-coated with gold. All the scaffolds were observed using a scanning electron microscope (Quanta 200, USA) at an accelerating voltage of 15 kV. Three scaffolds were tested and 10 randomly selected pores size/gap width in one SEM image of each scaffold. These images were manually measured and analyzed using Image J software v1.5 (NIH, Maryland, USA) to calculate the average pore size/gap width.

2.5. Atomic force microscope (AFM)

The scaffold was cut into a square of 1 × 1 cm and fixed on the mica sheet with double-sided adhesive. The whole material was placed on the loading platform for observation. The AFM observation was conducted in air at room temperature using the Bruker Dimension Icon System in noncontact mode. The probe model is SNL-A, the K value is 70 N/m, and the scanning rate is 1 Hz. Five different areas were randomly selected on each sample to confirm the consistency of the morphologies.

2.6. Fourier transform infrared (FTIR) spectroscopy

The scaffold material was scraped into powder with surgical blade, mixed with KBr at 1:100, and observed by tablet pressing. Fourier transforms infrared (FTIR) spectra were obtained from tablets containing samples and KBr with an FTIR spectrophotometer (Nicolet iS50; Thermo Fisher, USA). The FTIR spectra were recorded in the range of 400–4000 cm^{-1}, and the spectra plots represented the average of 32 scans. All measurements were carried out at room temperature.

2.7. X-ray diffraction (XRD) analyze

The scaffold material was scraped into powder with a surgical blade, and the powder was laid out in the grooves of the glass container, compacted and placed in the instrument for testing. Crystalline structure analysis was conducted using an X'Pert Pro X-ray diffractometer (Rigaku Mini Flex, Japan) with Cu Ka-radiation.

2.8. Thermal properties

10 mg sample was taken and put into crucible forceps for testing. Thermogravimetric analysis (TGA) of samples were scanned using a thermogravimetric analyzer (Mettler Toledo, TGA/DSC1 Star System) from 25 °C to 600 °C with a rate of 10 °C/min. The sample chamber was purged using nitrogen gas at 20 cm^3/min flow rate.

2.9. Hydrophilicity test

The hydrophilicity test was carried out by measuring the water absorption rate. Briefly, the samples were cut into squares with a length of 10 mm and measured the dry weight (W0), the samples were soaked in distilled water for 24 h and the wet weight (W1) of samples were measured. the water absorption rate was calculated by following equations:

$$\text{Water absorption rate}(\%) = \frac{W1 - W0}{W0} \times 100$$

Each test was conducted on five samples and the average was calculated.

2.10. Mechanical properties

Mechanical strength was tested by using a tensile testing machine (Instron-3345, Norwood, MA) at room temperature. The scaffolds (25 mm in length × 10 mm in width × (0.2–0.5) mm in thickness) were immersed in PBS for 2 h; then, they were pulled at a strain rate of 10 mm/min until rupture. The stress-strain curve was obtained to calculate the elastic modulus and maximum stress.

To test the suture strength, the suture (7–0; JinHuan, Shanghai, China) was inserted 2.0 mm from the edge of the short axis of the sample, looped, and secured with three knots. One end of the sample was fixed to the stage clamp of the uniaxial load test machine (Instron-3345), and the opposite sutured end was fixed to another clamp. The distance between the clamps was set at 2.0 cm. The sample was pulled at a 10 mm/min crosshead speed until rupture, and suture retention strength was calculated.

To test bursting strength, the sample was cut into square coupons (5.0 cm × 5.0 cm) and put on the rubber diaphragm of the pneumatic bursting strength tester (G229P). The appropriate test cup was selected before the test.

2.11. Flexibility test

The scaffolds (2.5 cm in length × 1.0 cm in width) were tested by twisted in the dry condition. The scaffolds (10.0 cm in length × 4.0 cm in width) were exhibited by different twisting angles in wet condition. To test the twistability and flexibility of both scaffolds, the samples (5.5 cm in length × 1.0 cm in width) were immersed in PBS buffer (pH = 7.4) for 30 min before testing; both sides were tightened with a needle holder, fixed on one side, and twisted on the other side, calculated the number of turns until they are broken. The wet scaffolds (4.0 cm in length × 1.0 cm in width) were tested using a tensile testing machine (HY-0580, Shanghai Hengyi Test Instrument CO, LTD) to measure cyclic tensile strain at room temperature. Five samples were tested for each group.

2.12. In vitro degradation of scaffolds

The resistance of the scaffolds against collagenase digestion was determined as previously described [21]. In brief, dry samples were cut into a square (1.0 cm × 1.0 cm) and weighted (W1), then incubated in collagenase solutions (1 U/mL) at 37 °C for 7, 14, 28 days. Samples were taken out from the solutions at each time point and were washed five times with distilled water. Then, the samples were lyophilized and weighed again (W2). The degradation rates of samples were calculated by the following equation:

$$\text{Degradation rate } (\%) = \frac{w1 - w2}{w1} \times 100$$

2.13. Cell adhesion, viability, and survival on both scaffolds

The scaffolds (diameter = 1.0 cm) were placed in 48-well plates. Murine L929 cells (3×10^3 cells/well), were cultured in 1640 Medium with 10% fetal bovine serum (FBS). The cells were cultured on the scaffolds for 1, 3, and 5 days to observe cell morphology. Cell cytoskeleton organization was visualized by fluorescently staining with phalloidin-AlexaFluor 488 (Sigma-Aldrich) and DAPI (Sigma-Aldrich). Images were taken by the laser scanning confocal microscope (Leica, Germany). Cell counting kit-8 (CCK-8) assay was applied to detect cell viability after culture for 1, 3, and 5 days. Cell survival was investigated by live/dead staining at 1, 3, and 5 days (Invitrogen Live/Dead kit), and

the quantification result was expressed as the following formula:

$$\text{Cell survival} = \frac{\text{The number of living cells}}{\text{The total number of living cells and dead cells}} \times 100\%$$

2.14. Characterization of cell infiltration and immune response in vivo

Animal experiments were approved by the Animal Experiments Ethical Committee of Nankai University and followed the Guide for Care and Use of Laboratory Animals. 6 adult male Sprague-Dawley rats (aged 8–10 weeks with a weight range of 250–280 g) were used for evaluating cell infiltration and immune response of both scaffolds. The circular scaffold (diameter = 1.0 cm, thickness = 200–300 μm) was sterilized with 75% ethanol and washed three times with PBS. Then, they were subcutaneously implanted into rats for 7 days and 28 days. DAPI staining and H&E staining were used to assess the cell infiltration; To identify macrophage phenotype, immunofluorescence staining was performed to classify macrophage phenotype with the following antibodies: CD68 (1:100, Abcam, ab31630), a general macrophage marker; inducible nitric oxide synthase (iNOS) (1:200, Abcam, ab15323), a marker for M1-like macrophages and CD206 (1:200, Abcam, ab64693) as a marker for M2-like macrophages. For immunofluorescence staining, thin frozen sections were incubated with 5% normal goat serum (Zhongshan Golden Bridge Biotechnology, China) for 30 min at room temperature. After reaction with primary antibodies in PBS overnight at 4 °C, the sections were incubated with secondary antibodies in PBS for 2 h at room temperature. The following secondary antibodies were used: goat anti-mouse IgG1 Alexa 488 (1:200, Invitrogen, USA) and goat anti-rabbit IgG Alexa 594 (1:200, Invitrogen, USA). The nuclei were counterstained with DAPI containing mounting solution (Southern Biotech, England). 5 views from middle position of each sample (3) were assessed. Images were observed with an epifluorescence microscope (Zeiss Axio Imager Z1, Germany).

2.15. In vivo implantation of scaffolds in a rat abdominal hernia defect model and corresponding evaluation

The surgical procedure referred to the methods previously reported by Hong et al. [22]. Briefly, a 3.5 cm incision was made 2.0 cm caudally below the xiphoid process in the midline of the abdomen, and a rectangular defect (1.0 × 2.5 cm) containing the fascia and rectus abdominis muscle (except for subcutaneous tissue and the skin) was created. This defect was reconstructed randomly with either Col-M or Col-A scaffolds. The scaffolds (27 mm in length × 12 mm in width × 0.5 mm in height) were sutured to the residual muscle by a continuous suture with 0.2 mm overlap between muscles and scaffolds, in direct contact with subcutaneous tissue and fascia transversalis. one defect was made per rat, and 3 rats were used in one group, and total 6 rats were used to evaluate the regenerative effects of both scaffolds. The skin was closed over the implanted scaffolds with a single lay suture. The implanted scaffolds were explanted at 4 weeks with representative specimens photographed *in situ*. The scaffolds were removed with the surrounding muscle by cutting approximately 0.5 cm from the original suture line along an apron border. For histochemical staining, the explanted scaffolds were embedded in optimal cutting temperature compound (OCT, Sakura, USA), quickly frozen in liquid nitrogen, and then cut into 6-μm sections. The sections were stained with Hematoxylin and Eosin (H&E, Solarbio, China) and Masson's trichrome (Solarbio, China). Images were observed with a brightfield microscope (Leica, DM3000, Germany). For immunofluorescent staining, frozen sections were fixed for 10 min using pre-cooled acetone, washed three times with PBS, and then incubated with 5% normal goat serum (Zhongshan Golden Bridge Biotechnology, China) for 30 min at room temperature. Then the sections were incubated with primary antibodies in PBS overnight at 4 °C, followed by incubation with secondary antibodies in PBS for 2 h at room temperature. All sections were rinsed 8 times in PBS between each step. Primary antibodies Anti-Von Willebrand Factor (1:200, Rabbit polyclonal antibody, Abcam, ab6994) and *Anti*-desmin (1:200 , Rabbit monoclonal, Abcam, ab32362) were used to characterize the vascularization and muscle regeneration. The following secondary antibodies were used: goat anti-mouse IgG1 Alexa 488 (1:200, Invitrogen, USA) and goat anti-rabbit IgG Alexa 488/594 (1:200, Invitrogen, USA). The nuclei were counterstained with DAPI containing mounting solution (Southern Biotech, England). Images were observed with an epifluorescence microscope (Zeiss Axio Imager Z1, Germany).

2.16. Statistical analysis

All quantitative results were collected from at least three samples. Data were displayed as the mean ± standard deviation of the mean (SD). All statistical analyses were performed in Graphpad Prism 8.0. The single comparison was carried out with an unpaired Student's t-test. Multiple comparisons were made using one-way analysis of variance (ANOVA) and Tukey's posthoc analysis. The minimum significance level was set at $P < 0.05$, $p < 0.01$, $p < 0.001$, $p < 0.0001$.

3. Results

3.1. Preparation and characterization of Col-A and Col-M scaffolds

Two scaffolds were fabricated using collagen molecules and collagen aggregates, through multiple steps, including vacuum homogenization, natural air drying, water soaking, lyophilization, and cross-linking (Fig. 2a). We firstly investigated the effect of crosslinker concentration on the mechanical strength of the scaffolds. The maximum strain decreased, whereas the maximum stress increased when the scaffolds were crosslinked with EDC and NHS (Supplementary Fig. 1a). The maximum stress of the scaffolds showed a trend of first increasing and then decreasing with the increase of cross-linker concentration. The scaffolds presented the highest maximum stress when the cross-linker concentration was 0.3% (m/v) (Fig. 2b). We then investigated the effects of freezing temperatures and soaking times on the scaffolds' mechanical properties and pore structure. The maximum tensile strength of the Col-M scaffolds was much lower than that of the Col-A scaffolds at the same freezing temperature or soaking time (Supplementary Fig. 1b). The freezing temperature (−20 °C and −80 °C) and soaking time (1hr and 3 hrs) had no significant effects on the mechanical properties of the two scaffolds treated with 0.3% crosslinker. The pore morphology of Col-M scaffolds is mostly irregular oval, while slender gaps distribute among the layers of Col-A scaffolds (Fig. 2c). At the same soaking time, the pore size of Col-M scaffolds and the gap width of Col-A scaffolds showed a decreased trend despite a noticeable difference, with the decrease in freezing temperature from −20 °C to −80 °C (Fig. 2d). The liquid nitrogen freezed Col-M and Col-A scaffolds are dense (Fig. 2c). The pore size of Col-M scaffolds increased with the increase of soaking time at the same freezing temperature (−20 °C or −80 °C) (Fig. 2d). However, the gap width of Col-A scaffolds decreased as the soaking time increased, displayed obvious difference at −20 °C and no significant difference at −80 °C (Fig. 2c, e). Based on the above-mentioned factors containing pore structure and mechanical strength, the scaffolds were fabricated with 0.3% crosslinker at −20 °C with soaking time of 1 h and used for further study.

Additionally, the two raw materials extracted from the bovine tendon were identified using AFM; the collagenous fibrils (381.6 ± 30.9 nm) exhibited a typical D-band pattern with a periodicity. However, the collagen molecules were composed of randomly distributed fine fibers with a diameter of 28.3 ± 8.3 nm. The surface of the Col-M scaffolds was smooth, while it was rough with randomly organized fibrils distributed on the surface of the Col-A scaffolds (Fig. 2f). Statistical results showed that the roughness of the Col-A scaffold was significantly higher than that of the Col-M scaffolds (Fig. 2g). X-ray diffraction showed two diffraction

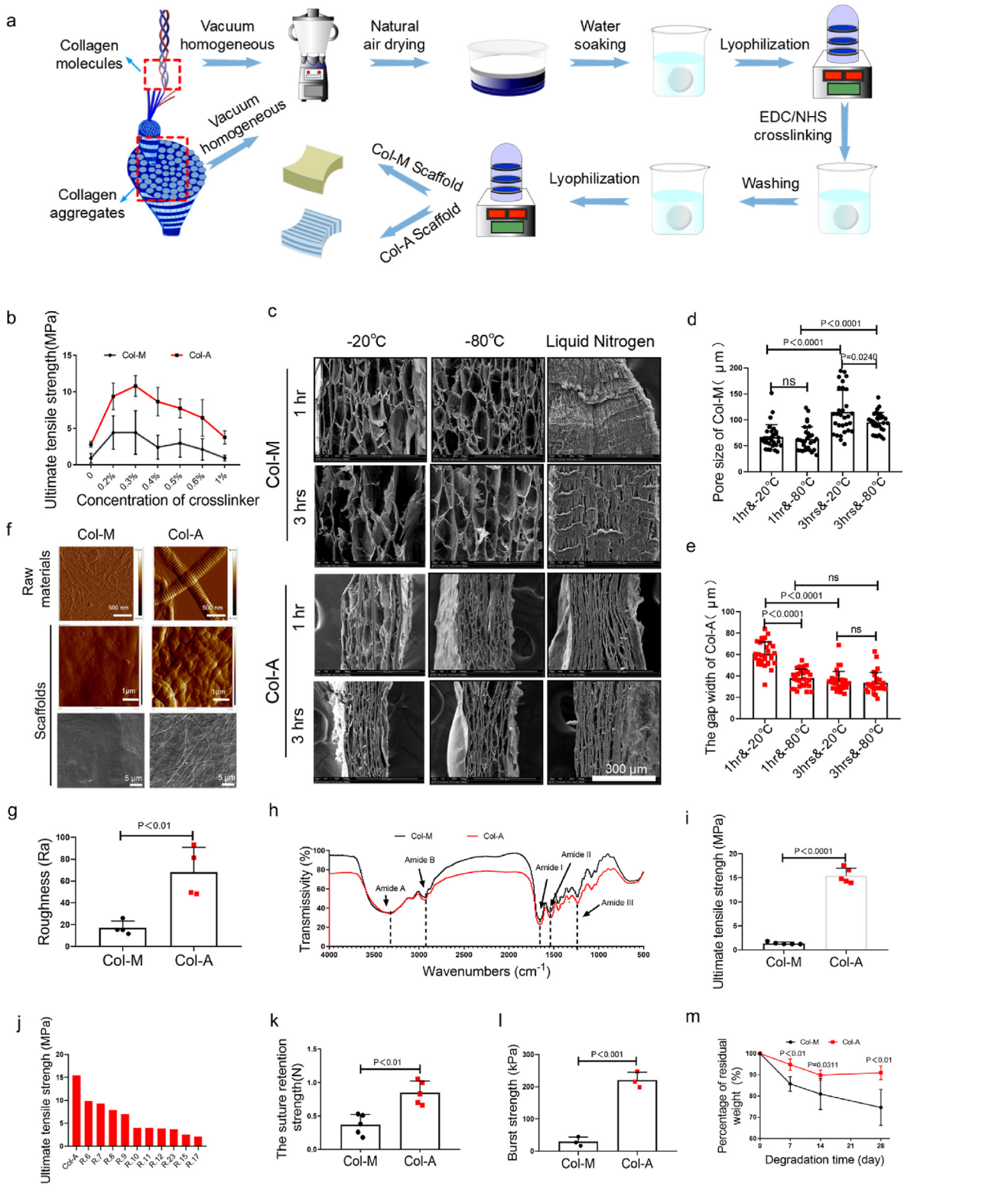

Fig. 2. Characterization of Col-A and Col-M scaffolds. (a) The fabrication process of Col-M and Col-A. (b) Comparison of the ultimate tensile strength of Col-M and Col-A scaffolds treated with different crosslinker concentrations (n = 5). (c) SEM demonstrates the effect of different freezing temperatures and immersion times on the pore structure of the Col-M and Col-A scaffold. (d, e) Pore size of the Col-M scaffold and the gap width of the Col-A scaffold treated with different freezing temperatures and immersion times (n = 30). (f) AFM images showing the microstructure of raw materials (upper row) and surface (lower row) of both scaffolds, SEM images showing the surface of scaffolds. (g) The roughness of both scaffold surfaces (n = 4). (h) FTIR spectra of both scaffolds. (i) The ultimate tensile strength of both scaffolds (n = 5). (j) Comparison of the Col-A scaffold with other-reported collagen scaffolds. (k, l) The suture retention (n = 5) and the burst strength (n = 3) of both scaffolds. (m) Enzymatic degradation of the Col-M and Col-A scaffolds after incubation in PBS with 1 U/mL collagenase for 7, 14, and 28 days at 37 °C. Bar heights and error bars represent means ± SD. Statistical analysis: Unpaired two-tailed Student's t-test. ns = no significance. Scale bar: c, 300 μm; f, 500 nm (upper row); 1 μm (middle row); 5 μm (lower row).

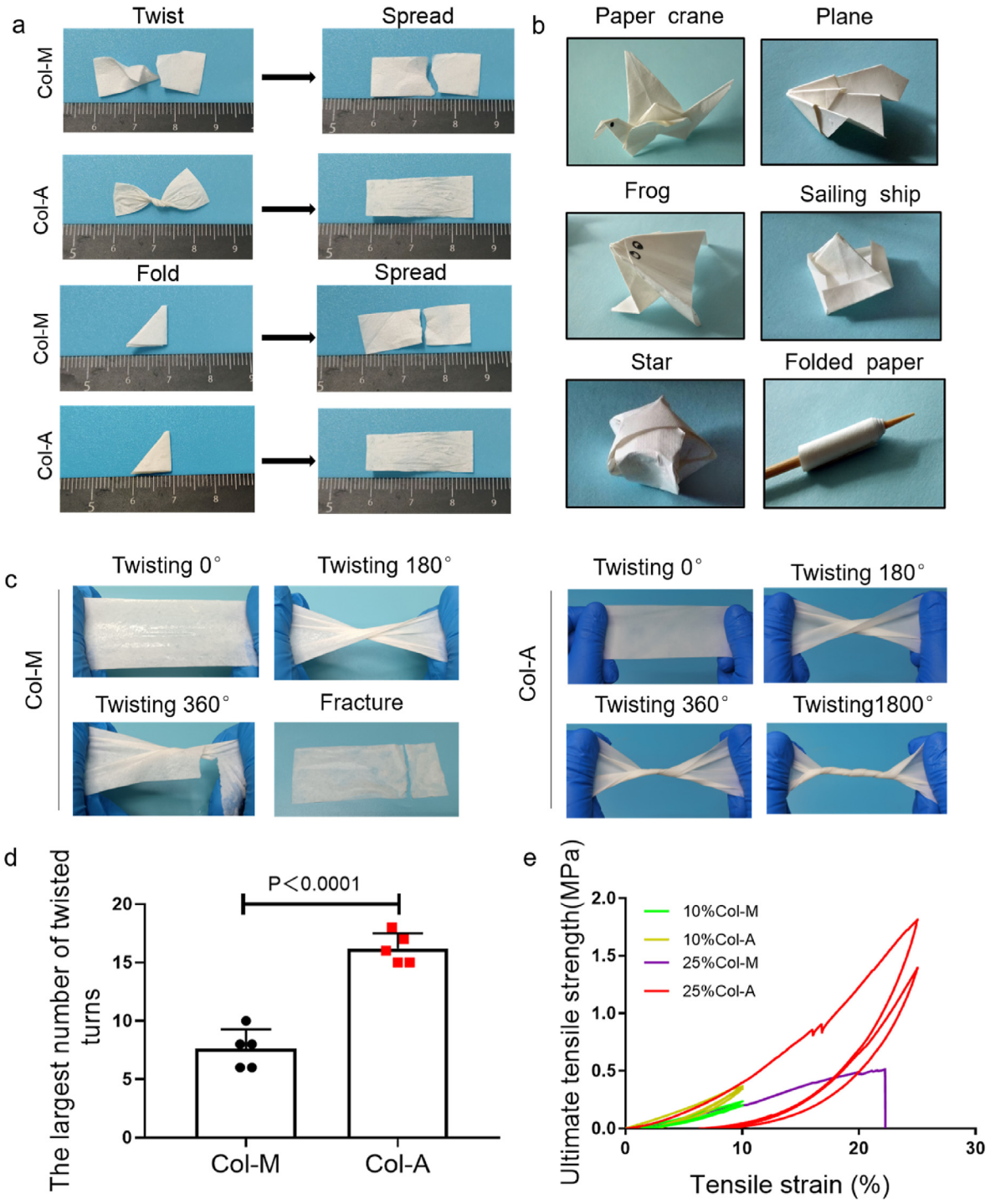

Fig. 3. The flexibility of the Col-M and Col-A scaffold. (a) Photographs of the dry scaffolds after twisting and folding. (b) The dry Col-A scaffold is folded into different shapes. (c) Photographs of the wet scaffolds with different twisting angles. (d) Comparison of the largest number of twisted turns of the wet scaffolds twisting until fracture (n = 5). (e) Comparison of the stress-strain curve of the scaffolds at 10% or 25% deformation under cyclic loading. Bar heights and error bars represent means ± SD. Statistical analysis: Unpaired two-tailed Student's t-test.

peaks at 2θ = 7–8° and 21°, indicating triple helix structure of collagen (Supplementary Fig. 2) [21]. The FTIR spectroscopy was performed to characterize two scaffolds as shown in Fig. 2h. The typical absorption bands at 3300 $cm^{-1}$and 2930 cm^{-1} represent amide A and amide B are caused by the stretching vibration of N–H (Fig. 2h) [11]. Further, the maximum tensile strength of Col-A scaffolds was obviously higher than that of Col-M scaffolds (Fig. 2i). The maximum tensile strength of the Col-A scaffolds was significantly higher than that of the reported collagen scaffolds made of collagen molecules (Fig. 2j) [6–12,16,17,23]. The suture strength of the Col-A scaffold (0.85 ± 0.17 N) was significantly higher than that of the Col-M scaffolds (0.37 ± 0.15 N) (Fig. 2k). The burst strength of the Col-A scaffolds (220.7 ± 24.8 kPa) was much higher than that of the Col-M scaffolds (29.6 ± 14.4 kPa) (Fig. 2l).

Thermogravimetric and micro-quotient thermogravimetric tests showed that both scaffolds displayed the same weight loss phase (30–150 °C and 250–500 °C), and the residual amount of the Col-A scaffold was slightly higher than that of the Col-M scaffold (Supplementary Figs. 3a and b).

In vitro, enzymatic degradation assessments showed that the weight loss of the Col-A scaffolds was significantly lower than that of the Col-M scaffolds over time, and the percentage of the residual weight of both scaffolds was 90.96 ± 3.21% and 74.66 ± 0.48% at 28 days, respectively (Fig. 2m).

The water absorption rate of the uncross-linked Col-M scaffolds was considerably higher than that of the Col-A scaffolds at 24 h, and no noticeable difference was observed in the water absorption between the two cross-linked scaffolds (Supplementary Figs. 4a and b).

3.2. Flexibility of two scaffolds in the dry and wet conditions

We first characterized the flexibility of both scaffolds in the dry condition. The Col-A scaffolds were twisted at 720° without tearing, while the Col-M scaffolds were torn after being twisted at 180° (Fig. 3a). Moreover, the Col-M scaffolds ruptured only after 4 folds, however, no fracture occurred even after folding 100 times in Col-A scaffolds (Fig. 3a). Further, the Col-A scaffolds can be folded into almost any shape, including a crane, plane, frog, sailing ship, star, and a roll of paper (Fig. 3b). Although Col-M scaffolds can also be folded into these shapes, they are prone to tearing (data not shown). We then twisted the two scaffolds in the wet condition, and the Col-M scaffold fractured upon twisting at 360°, while no fracture was observed for the Col-A scaffolds upon twisting at 1800° (Fig. 3c). The statistical results showed that the largest number of Col-A scaffolds' twisted turns were significantly higher than Col-M (Fig. 3d). No fracture occurred when both scaffolds were treated with 5 times cyclic loading after a 10% deformation. Col-A scaffolds can stand 25% deformation. However, the Col-M scaffolds fractured immediately under first cyclic loading (Fig. 3e).

3.3. Cell behaviors regulated by Col-A and Col-M scaffolds in vitro

The cell adhesion, survival, and proliferation effect of Col-A on cells was investigated *in vitro* in comparison to that of Col-M. As shown in Fig. 4a, Phalloidin staining showed that on day 1, L929 cells adhered and spread on both scaffolds, and cells on the Col-A scaffold exhibited a more elongated morphology compared to the Col-M scaffolds. On days 3 and 5, cell density increased on both scaffolds, cells on the Col-A scaffold still exhibiting an elongated morphology, while the cells on the Col-M scaffolds exhibited a more rounded shape. The statistical data further confirmed the above results, the aspect ratio of cells on Col-A scaffolds was much higher than that on Col-M scaffolds (Fig. 4b). It was observed by SEM that the cells were more spreading and elongated on the Col-A scaffold, while the cells on the Col-M scaffolds mostly displayed a round shape (Fig. 4c). On day 1, the CCK8 assay showed that the OD values of the cells on Col-A was lower than that on Col-M and control group, with no noticeable difference between Col-A and Col-M group. On day 3 and 5, the absorption values of the cells on the Col-A scaffolds were

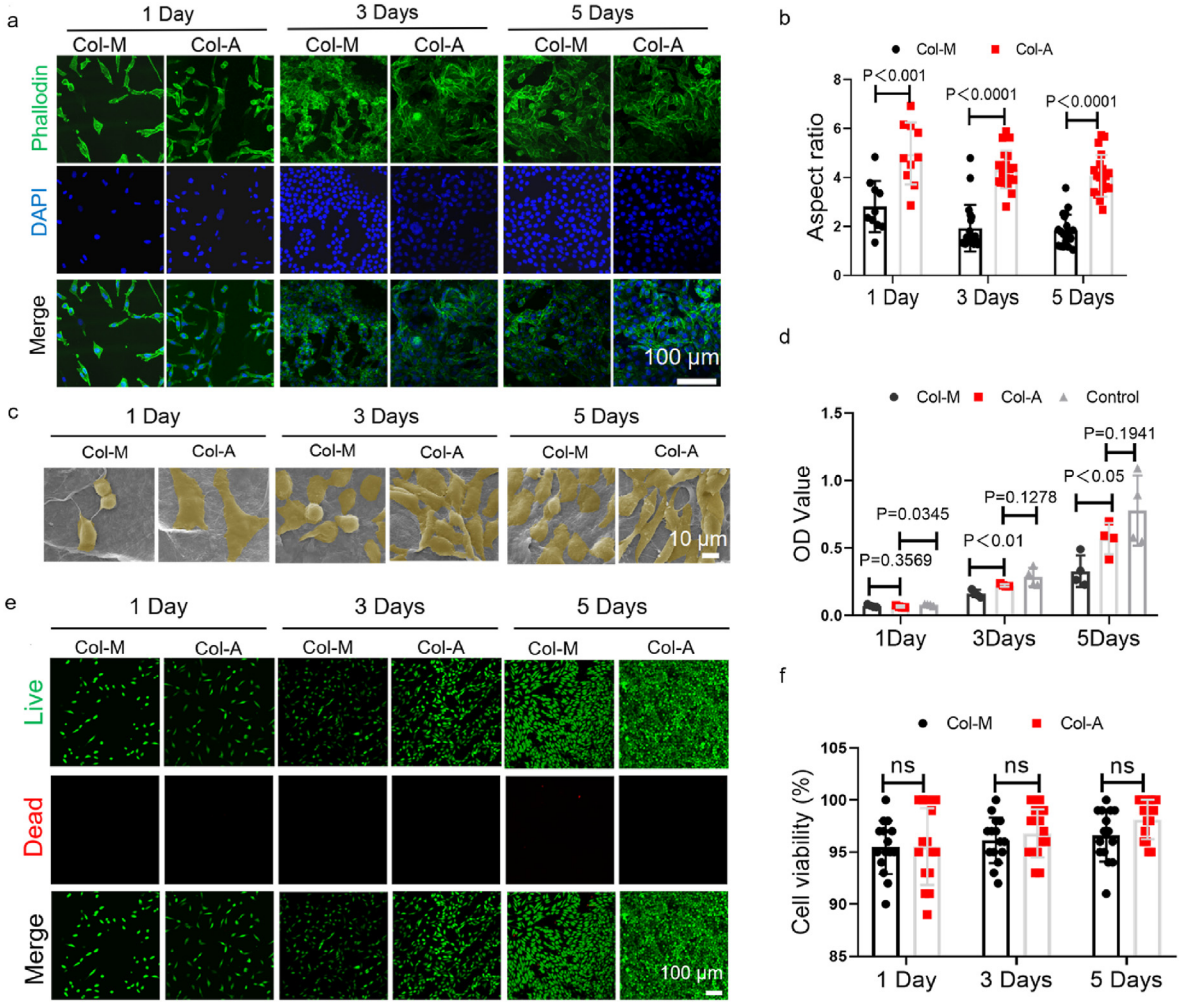

Fig. 4. Cellular regulatory effects of the Col-M and Col-A scaffolds cultured for 1, 3, and 5 days. (a) DAPI/phalloidin staining of both scaffolds; (b) Aspect ratio in the DAPI/phalloidin images. (c) The SEM images showing cell morphology on both scaffolds. (d) Cell proliferation on both scaffolds and control group was determined by the CCK8 assay. (e, f) Cell viability on both scaffolds was assessed by live/dead staining. Bar heights and error bars represent means ± SD. Statistical analysis: Unpaired two-tailed Student's t-test. ns = no significance. Scale bar: a, 100 μm; c, 10 μm; e, 100 μm.

obviously higher than those on the Col-M scaffolds, and they all presented a rising trend, no significant difference was observed between Col-A scaffolds and control group (Fig. 4d). Live/dead cell assays showed that cell survival on both scaffolds was higher than 95%, no significant difference was observed on days 1, 3, and 5 (Fig. 4e and f).

3.4. Cell infiltration and immunogenic properties of the Col-M and Col-A scaffolds in vivo

Both Col-A and Col-M scaffolds were implanted into rat subcutaneous models for 7 and 28 days to evaluate the cellular infiltration and immune response. DAPI and H&E staining showed that the number of host cells migrated into the interior of the Col-A scaffolds gradually increased over time, however, the cells were mostly still distributed at the edge of the Col-M scaffold even at 28 days (Fig. 5a, b, c). Macrophages (CD68-positive) can be polarized between iNOS-positive pro-inflammatory macrophages (M1) and CD206-positive anti-inflammatory macrophages (M2). Immunostaining for these markers confirmed that CD206/CD68-positive cells were distributed both inside and outside the Col-A scaffolds and only near the peripheral border of the Col-M scaffolds (Fig. 5d). Statistically, the number of M2-type cells in the Col-A scaffolds was significantly higher than that in the Col-M scaffolds at 7 and 28 days (Fig. 5e). There were few iNOS/CD68-positive cells at both 7 and 28 days, and no statistical difference was observed between both scaffolds (Fig. 5f and g).

3.5. Rectus abdominis muscle regeneration after implantation of Col-A and Col-M scaffolds in rat's model

A rat hernia model was used to verify both scaffolds' mechanical stability and pro-regenerative properties (Fig. 6a). Both scaffolds were explanted after one-month post-implantation into the rat abdominal muscle hernia defect. Col-M scaffolds guided thin neo-muscle regeneration (1.3 ± 0.3 mm), and the corresponding implantation site was bulging and protruding, showing a risk of re-herniation. However, neo-muscle regeneration guided by Col-A scaffolds was thick (2.0 ± 0.5 mm), and its volume was close to the defect area (Fig. 6b). H&E staining further confirmed that the neo-tissue guided Col-M scaffolds were thin, broken, and discontinuous. In contrast, thick neo-muscles guided by the Col-A scaffolds were continuous and homogeneous (Fig. 6c). The statistical results showed that the thickness of regenerated tissue guided by the Col-A scaffold was ominously higher than that of Col-M scaffolds (Fig. 6d). Masson staining revealed a large number of collagen fibers at the implantation site of Col-M scaffolds. In contrast, a large amount of new muscle accompanied by a small amount of collagen is distributed at the implantation site of Col-A scaffolds (Fig. 6e). Accordingly, the average percentage of muscle fiber area of new muscle guided by Col-A scaffolds (83.8 ± 8.2%) was statistically higher than that of Col-M scaffolds (61.9 ± 9.6%) (Fig. 6f). The collagen deposition area (16.2 ± 3.1%) in the Col-A group was significantly lower than that of Col-M scaffolds (38.1 ± 8.9%). Desmin staining and its statistical results further proved that significantly higher myofiber density was observed in the Col-A scaffolds implantation site than that in the Col-M scaffolds (86.6 ± 15.1% vs 51.8 ± 26.6%) (Fig. 6g). *Anti*-vWF antibody staining showed that the number of capillaries in the Col-A scaffolds was significantly higher than that of the Col-M scaffolds (Fig. 6h and i). Immunofluorescence staining showed that the number of CD206 positive cells in the Col-A scaffolds was significantly higher than that in Col-M scaffolds (Supplementary Figs. 5a and b).

4. Discussion

The lack of sufficient mechanical strength and flexibility of collagen-based scaffolds limits promotive effect on tissue regeneration [2,4]. We prepared high-strength, porous, and flexible collagen-based scaffolds using collagen aggregates combined with vacuum homogenization, natural air-drying, water soaking, lyophilization, and cross-linking processes. Compared with Col-M scaffolds, Col-A scaffolds enabled cell adhesion, spreading, proliferation, migration, and macrophage polarization *in vivo*, and promoted muscle regeneration and vascularization in the rat model of ventral hernia.

Tough Col-A scaffolds were fabricated by combining paper-making technology with pore-making and cross-linking technology. Compared with the dense collagen scaffolds prepared by the multi-cyclic parallel directional flow casting method (9.38 MPa) [7] or multiple unconfined compression methods (2.1 MPa) [17], the Col-A scaffolds not only possess a high tensile strength (15.46 MPa), but also retain a porous structure and flexibility. Meanwhile, this method is simple and easy to implement and control. The mechanical strength of collagen scaffolds can be effectively improved by using collagen of high structural levels, thus providing the basis for the large-scale production of collagen-based materials for clinical application.

The scaffolds should have tough mechanical strength, suitable pore structure, and high flexibility, providing appropriate physical support for tissue repair [22,24–26]. The mechanical strength of the Col-A scaffold without the formation of pore structure is much higher than that of collagen-based scaffolds reported in the literature (22.45 MPa vs 18.45 MPa [16]). The appropriate pore structure inside the scaffolds is a critical factor in promoting cellularization and tissue integration [5]. Therefore, the Col-A scaffolds with pore structures were constructed and controlled by water soaking and lyophilization. Although the pore structure reduced the mechanical strength, the ultimate tensile strength of the Col-A scaffold is well above 15 MPa, which has not been reported so far. Meanwhile, its suture retention strength and burst strength are significantly higher than that of Col-M scaffolds. This is mainly attributed to the choice of the thick collagen fibrils as raw materials used for fabricating Col-A scaffolds. It also offers the Col-A scaffolds with multi-layered mechanical protection under external forces containing the longitudinal elongation of the fibrils, an increase in the gap distance in the D-band pattern of fibrils, and the straightening of the triple helix structure of the collagen molecules. In contrast, the Col-M scaffolds will rupture under small deformations because of the little mechanical protection of the multi-layered structure [19,27]. In addition, the pore wall thickness in the Col-A scaffold is significantly higher than that of the Col-M scaffolds, which also contributes to its mechanical strength. The influence of material density and pore size on mechanical strength of both scaffolds is also not excluded.

Enhanced flexibility of Col-A scaffolds is expected to provide efficient support for a broader range of applications, especially in the clinical setting [28,29]. The flexibility of the Col-A scaffolds is much higher than that of the Col-M scaffolds, which was also mainly attributed to high level structure of collagen aggregates [19]. More importantly, no bulging, protrusion, or rupture occurred in the Col-A scaffolds at 1 month in the rat hernia defect model, which validates their mechanical performance in promoting tissue repair.

The scaffolds possessing good cytocompatibility and histocompatibility support cell adhesion, migration, and proliferation and thus improve tissue repair [30,31]. Both scaffolds displayed good cytocompatibility. Fibroblasts exhibited a stretched state on the Col-A scaffolds but rounded on the Col-M scaffolds. The reason is that the Col-A scaffolds composed of large amounts of collagen fibrils increased their surface roughness, while the surface of the Col-M scaffold tends to be smooth. Numerous studies have presented that rough surfaces have more beneficial binding sites for cell adhesion and spreading than smooth surfaces [6,32]. Because EDC and NHS are zero-length chemical cross-linkers, they have little effect on the cytocompatibility of the scaffolds through thorough washing [33]. The Col-A scaffolds significantly increased cell infiltration compared with the Col-M scaffolds for the reason that the elongated pore structure, large pore size, and thick

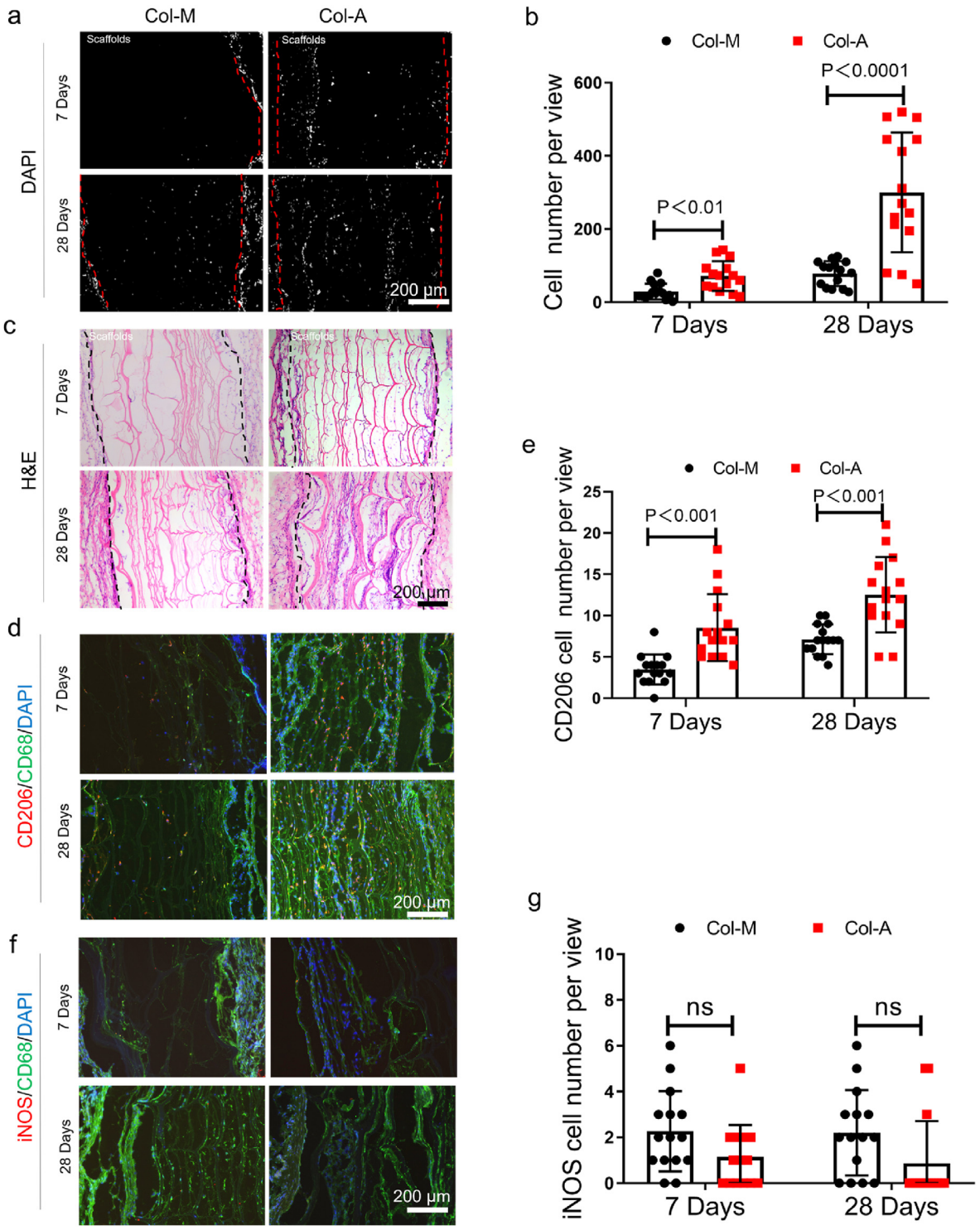

Fig. 5. Cell infiltration and immunogenic properties of the Col-M and Col-A scaffolds in a rat subcutaneous implantation model at 7 and 28 days. (a) DAPI staining of the cross-sections showing cell infiltration within the scaffolds. (b) Quantification of cells within the scaffolds (n = 15). The red dotted line indicates the edge of the scaffolds. (c) Optical images of cross-sections stained with H&E showing cellularization. The black dotted line indicates the edge of the scaffolds. (d) Macrophages were detected by co-immunofluorescence staining for CD206 (red, anti-inflammatory)/CD68 (green, pan-macrophage). (e) Quantification of CD206-positive cells within the scaffolds (n = 15). (f) Macrophages were detected by co-immunofluorescence staining for iNOS (red, anti-inflammatory)/CD68 (green, pan-macrophage). (g) Quantification of iNOS-positive cells within the scaffolds (n = 15). Images and data are representative of n = 3 individual experiments, and bar heights and error bars represent means ± SD. Statistical analysis: Unpaired two-tailed Student's t-test. ns = no significance. Scale bar: a, c, d, f, 200 μm. (For interpretation of the references to colour in this figure legend, the reader is referred to the Web version of this article.)

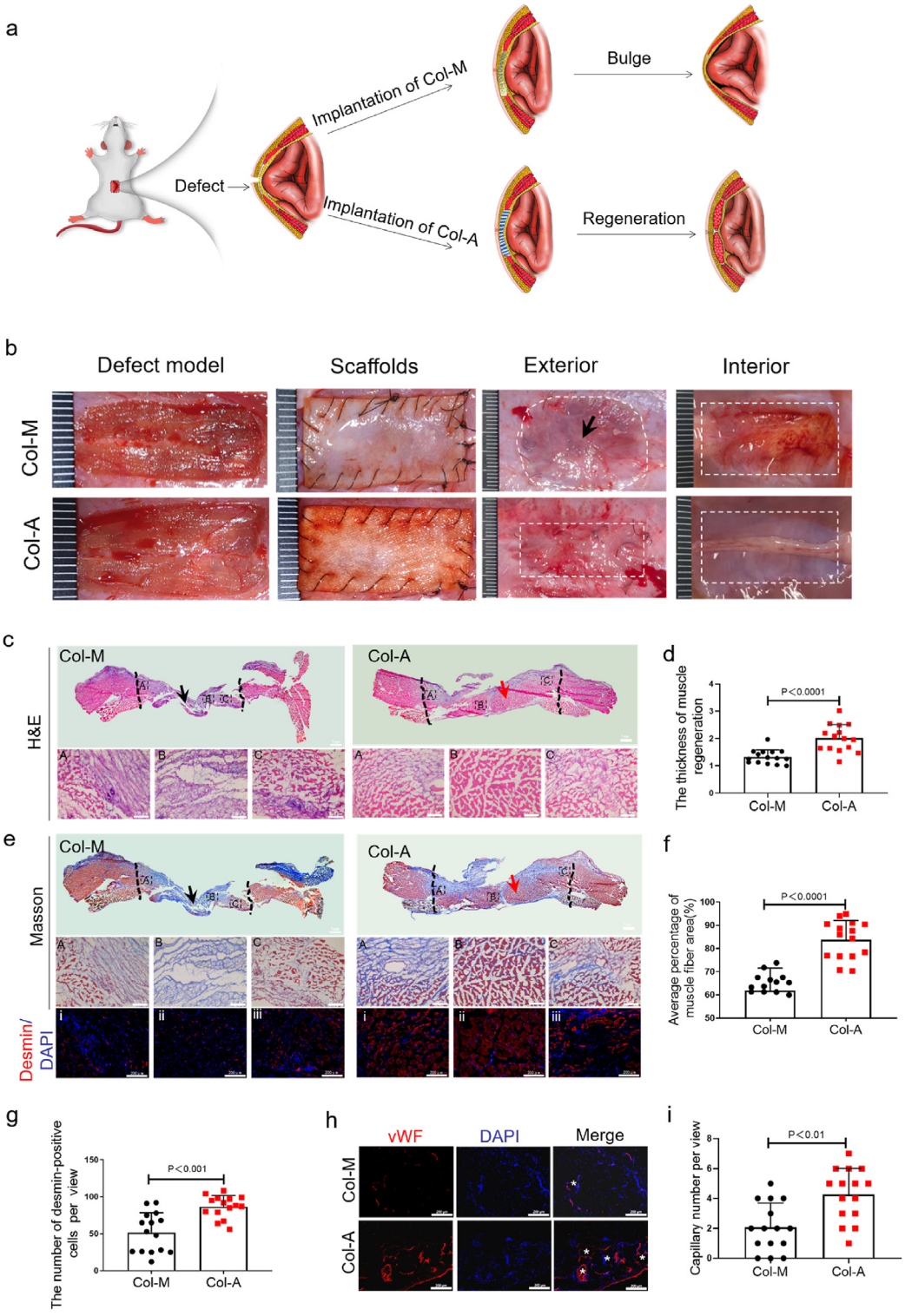

Fig. 6. *In vivo* muscle regeneration guided by Col-M and Col-A scaffolds after 1-month implantation in the rat rectus abdominis defects model. (a) Schematic illustration of implantation and regeneration of the scaffolds. (b) Defects models, implantation, and explantation of the regenerated scaffolds. The white dotted line indicates the edge of the defects. (c) H&E staining of the explanted scaffolds showing muscle regeneration. (d) Statistics of the thickness of the regenerated muscle. (e) Masson trichrome staining and immunofluorescence staining (desmin, red) showing the functional muscle fibers formation. The black dotted line indicates the edge of the defects. The black arrow indicates the bulge. The red arrow indicates the regeneration. (f) Statistics of the average percentage of muscle fibers area (n = 15). (g) The number of desmin-positive cells per view (n = 15). (h) Immunofluorescence staining of vWF antibody showing the capillaries formation. The white asterisks indicate the capillaries. (i) Number of capillaries per view (n = 15). Bar heights and error bars represent means ± SD. Statistical analysis: Unpaired two-tailed student's t-test. Scale bar: c, 1 mm (upper image), 200 μm (lower image); e, Masson, 1 mm (upper image), 200 μm (lower image); Desimin, 200 μm h, 200 μm. (For interpretation of the references to colour in this figure legend, the reader is referred to the Web version of this article.)

pore wall in the Col-A scaffold enabled cells migration [24]. In addition, the Col-A scaffolds promoted the M2-type polarization of macrophages compared with the Col-M scaffold. Several studies also showed that scaffolds' elongated pore structure and nanofibers could switch macrophage polarization [34,35]. M2 macrophages have been proven to enhance tissue repair, which has been confirmed in muscle regeneration and vascularization in a rat hernia model [36,37].

There are still some issues to be investigated in further study. For instance, interrelation of pore size or density of the collagen slurry and mechanical properties is worthy of studying. Functionalizing the Col-A scaffolds (e.g., antibacterial, electrical conductivity, mineralization, etc.) will offer more application scenarios. In addition, the regenerative effect of Col-A scaffolds on the repair of other tissues and large animal models (Achilles tendon, ligaments, etc.) is yet to be tested.

5. Conclusion

In summary, we developed a high -strength, flexible, and porous collagen-based scaffolds using collagen aggregates as raw materials. The Col-A scaffolds demonstrated good cytocompatibility and histocompatibility and the capability of regenerating the rectus abdominis muscle in the rat model. Our study provides a novel approach to the development of collagen-based materials. Also, it broadens the scope of the clinical application of collagen-based scaffolds in tissue regeneration.

Credit author statement

M.F.Z. and **W·H.D.** conceived the research; **M.F.Z. X.T.H** and **W·H.D.** designed the experiments; **X.T.H** designed, fabricated and characterized scaffolds; **X.T.H, W.L.** and **Y.L.** performed cell experiments. **X.T.H. S·Y.L.** and **Y·N·C** performed microsurgery of animal experiments. **M.F.Z, N·H.D**, and **X.T.H.** analyzed the data and wrote the manuscript. All authors discussed the data and direction of the project at regular intervals throughout the study.

Funding

This work was supported by the National Natural Science Foundation of China (NSFC) projects (81972063, 81701840); we thank the Haihe Laboratory of Sustainable Chemical Transformations for financial support; The Opening Project of Key Laboratory of Leather Chemistry and Engineering, Sichuan University, Ministry of Education (SCU2021D005); Science and Technology Planning Project of Tianjin (19ZXYXSY00070).

Declaration

All authors declare no competing interests.

Data availability

The data in this work are available in the manuscript or Supplementary Information, or available from the corresponding author upon reasonable request.

Declaration of competing interest

The authors declare that they have no known competing financial interests or personal relationships that could have appeared to influence the work reported in this paper.

Appendix A. Supplementary data

Supplementary data to this article can be found online at https://doi.org/10.1016/j.mtbio.2022.100376.

References

[1] K. Lin, D. Zhang, M.H. Macedo, W. Cui, B. Sarmento, G. Shen, Advanced collagen-based biomaterials for regenerative biomedicine, Adv. Funct. Mater. 29 (3) (2019).
[2] L. Gu, T. Shan, Y.X. Ma, F.R. Tay, L. Niu, Novel biomedical applications of crosslinked collagen, Trends Biotechnol. 37 (5) (2019) 464–491.
[3] V.A. Patil, K.S. Masters, Engineered collagen matrices, Bioengineering (Basel) 7 (4) (2020).
[4] A. Sorushanova, L.M. Delgado, Z. Wu, N. Shologu, A. Kshirsagar, R. Raghunath, A.M. Mullen, Y. Bayon, A. Pandit, M. Raghunath, D.I. Zeugolis, The collagen suprafamily: from biosynthesis to advanced biomaterial development, Adv Mater 31 (1) (2019), e1801651.
[5] M. Zhu, W. Li, X. Dong, X. Yuan, A.C. Midgley, H. Chang, Y. Wang, H. Wang, K. Wang, P.X. Ma, H. Wang, D. Kong, In vivo engineered extracellular matrix scaffolds with instructive niches for oriented tissue regeneration, Nat. Commun. 10 (1) (2019) 4620.
[6] Y. Liu, L. Ren, Y. Wang, A novel collagen film with micro-rough surface structure for corneal epithelial repair fabricated by freeze drying technique, Appl. Surf. Sci. 301 (2014) 396–400.
[7] Y. Tanaka, K. Baba, T.J. Duncan, A. Kubota, T. Asahi, A.J. Quantock, M. Yamato, T. Okano, K. Nishida, Transparent, tough collagen laminates prepared by oriented flow casting, multi-cyclic vitrification and chemical cross-linking, Biomaterials 32 (13) (2011) 3358–3366.
[8] Y. Liu, H. Lv, L. Ren, G. Xue, Y. Wang, Improving the moisturizing properties of collagen film by surface grafting of chondroitin sulfate for corneal tissue engineering, J. Biomater. Sci. Polym. Ed. 27 (8) (2016) 758–772.
[9] X. Chen, L. Zhou, H. Xu, M. Yamamoto, M. Shinoda, I. Tada, S. Minami, K. Urayama, H. Yamane, The structure and properties of natural sheep casing and artificial films prepared from natural collagen with various crosslinking treatments, Int. J. Biol. Macromol. 135 (2019) 959–968.
[10] W. Wang, Y. Zhang, R. Ye, Y. Ni, Physical crosslinkings of edible collagen casing, Int. J. Biol. Macromol. 81 (2015) 920–925.
[11] D. Shi, F. Liu, Z. Yu, B. Chang, H.D. Goff, F. Zhong, Effect of aging treatment on the physicochemical properties of collagen films, Food Hydrocolloids 87 (2019) 436–447.
[12] A. Satyam, G.S. Subramanian, M. Raghunath, A. Pandit, D.I. Zeugolis, In vitro evaluation of Ficoll-enriched and genipin-stabilised collagen scaffolds, J Tissue Eng Regen Med 8 (3) (2014) 233–241.
[13] Y. Ma, W. Wang, Y. Wang, Y. Guo, S. Duan, K. Zhao, S. Li, Metal ions increase mechanical strength and barrier properties of collagen-sodium polyacrylate composite films, Int. J. Biol. Macromol. 119 (2018) 15–22.
[14] K. Liang, E. Spiesz, D. Schmieden, A. Xu, A. Meyer, M.J.A.n. Aubin-Tam, Bioproduced Polymers Self-Assemble with Graphene Oxide into Nanocomposite Films with Enhanced Mechanical Performance, vol. 14, 2020, pp. 14731–14739, 11.
[15] X. Wu, A. Liu, W. Wang, R. Ye, Improved mechanical properties and thermal-stability of collagen fiber based film by crosslinking with casein, keratin or SPI: effect of crosslinking process and concentrations of proteins, Int. J. Biol. Macromol. 109 (2018) 1319–1328.
[16] S. Yang, X. Shi, X. Li, J. Wang, Y. Wang, Y. Luo, Oriented collagen fiber membranes formed through counter-rotating extrusion and their application in tendon regeneration, Biomaterials 207 (2019) 61–75.
[17] E. Abou Neel, U. Cheema, J. Knowles, R. Brown, S.J.S.m. Nazhat, Use of Multiple Unconfined Compression for Control of Collagen Gel Scaffold Density and Mechanical Properties, vol. 2, 2006, pp. 986–992, 11.
[18] J. Puetzer, T. Ma, I. Sallent, A. Gelmi, M.J.B. Stevens, Driving hierarchical collagen fiber formation for functional tendon, Ligament, and Meniscus Replacement 269 (2021), 120527.
[19] A. Gautieri, S. Vesentini, A. Redaelli, M.J. Buehler, Hierarchical structure and nanomechanics of collagen microfibrils from the atomistic scale up, Nano Lett. 11 (2) (2011) 757–766.
[20] X. Liu, N. Dan, W. Dan, Preparation and characterization of an advanced collagen aggregate from porcine acellular dermal matrix, Int. J. Biol. Macromol. 88 (2016) 179–188.
[21] Y. Chen, N. Dan, L. Wang, X. Liu, W. Dan, Study on the cross-linking effect of a natural derived oxidized chitosan oligosaccharide on the porcine acellular dermal matrix, RSC Adv. 6 (44) (2016) 38052–38063.
[22] Y. Hong, A. Huber, K. Takanari, N.J. Amoroso, R. Hashizume, S.F. Badylak, W.R. Wagner, Mechanical properties and in vivo behavior of a biodegradable synthetic polymer microfiber-extracellular matrix hydrogel biohybrid scaffold, Biomaterials 32 (13) (2011) 3387–3394.
[23] K.-R. Zhang, H.-L. Gao, X.-F. Pan, P. Zhou, X. Xing, R. Xu, Z. Pan, S. Wang, Y. Zhu, B. Hu, D. Zou, S.-H. Yu, Multifunctional bilayer nanocomposite guided bone regeneration membrane, Matter 1 (3) (2019) 770–781.
[24] W. Su, Y. Ran, L. Ma, X. Ma, Z. Yi, G. Chen, X. Chen, Z. Deng, Q. Tong, X. Li, Micro-/Nanomechanics dependence of biomimetic matrices upon collagen-based fibrillar aggregation and arrangement, Biomacromolecules 21 (9) (2020) 3547–3560.
[25] L. Zhang, S. Gopalakrishnan, K. Li, L.S. Wang, Y. Han, V.M. Rotello, Fabrication of collagen films with enhanced mechanical and enzymatic stability through thermal treatment in fluorous media, ACS Appl. Mater. Interfaces 12 (5) (2020) 6590–6597.
[26] H.C. Wells, K.H. Sizeland, N. Kirby, A. Hawley, S. Mudie, R.G. Haverkamp, Collagen fibril structure and strength in acellular dermal matrix materials of bovine, porcine, and human origin, ACS Biomater. Sci. Eng. 1 (10) (2015) 1026–1038.
[27] M.J. Buehler, Nature Designs Tough Collagen: Explaining the Nanostructure of Collagen Fibrils, 2006.

[28] J. Chen, T. Ahn, I.D. Colon-Bernal, J. Kim, M.M. Banaszak Holl, The relationship of collagen structural and compositional heterogeneity to tissue mechanical properties: a chemical perspective, ACS Nano 11 (11) (2017) 10665–10671.
[29] K. Tai, M. Dao, S. Suresh, A. Palazoglu, C. Ortiz, Nanoscale heterogeneity promotes energy dissipation in bone, Nat. Mater. 6 (6) (2007) 454–462.
[30] A.K. Gaharwar, I. Singh, A. Khademhosseini, Engineered biomaterials for in situ tissue regeneration, Nat. Rev. Mater. 5 (9) (2020) 686–705.
[31] N. Mitrousis, A. Fokina, M.S. Shoichet, Biomaterials for cell transplantation, Nat. Rev. Mater. 3 (11) (2018) 441–456.
[32] C.N. Grover, J.H. Gwynne, N. Pugh, S. Hamaia, R.W. Farndale, S.M. Best, R.E. Cameron, Crosslinking and composition influence the surface properties, mechanical stiffness and cell reactivity of collagen-based films, Acta Biomater. 8 (8) (2012) 3080–3090.
[33] M.M. Islam, D.B. AbuSamra, A. Chivu, P. Argueso, C.H. Dohlman, H.K. Patra, J. Chodosh, M. Gonzalez-Andrades, Optimization of collagen chemical crosslinking to restore biocompatibility of tissue-engineered scaffolds, Pharmaceutics 13 (6) (2021).
[34] L. Rabiller, V. Robert, A. Arlat, E. Labit, M. Ousset, M. Salon, A. Coste, L. Da Costa-Fernandes, P. Monsarrat, B. Segui, M. Andre, C. Guissard, M.L. Renoud, M. Silva, G. Mithieux, I. Raymond-Letron, L. Penicaud, A. Lorsignol, L. Casteilla, C. Dromard Berthezene, B. Cousin, Driving regeneration, instead of healing, in adult mammals: the decisive role of resident macrophages through efferocytosis, NPJ Regen Med 6 (1) (2021) 41.
[35] Z. Wang, Y. Cui, J. Wang, X. Yang, Y. Wu, K. Wang, X. Gao, D. Li, Y. Li, X.L. Zheng, Y. Zhu, D. Kong, Q. Zhao, The effect of thick fibers and large pores of electrospun poly(epsilon-caprolactone) vascular grafts on macrophage polarization and arterial regeneration, Biomaterials 35 (22) (2014) 5700–5710.
[36] B.N. Brown, R. Londono, S. Tottey, L. Zhang, K.A. Kukla, M.T. Wolf, K.A. Daly, J.E. Reing, S.F. Badylak, Macrophage phenotype as a predictor of constructive remodeling following the implantation of biologically derived surgical mesh materials, Acta Biomater. 8 (3) (2012) 978–987.
[37] M.O. Dellacherie, B.R. Seo, D.J. Mooney, Macroscale biomaterials strategies for local immunomodulation, Nat. Rev. Mater. 4 (6) (2019) 379–397.